ELSEVIER

Nuclear Instruments and Methods in Physics Research A 387 (1997) 352-364

NUCLEAR INSTRUMENTS & METHODS IN PHYSICS RESEARCH Section A

Test beam performance of the electromagnetic calorimeter of the NOMAD experiment

D. Autiero[a,1], M. Baldo-Ceolin[b], F. Bobisut[b], P.W. Cattaneo[c], L. Camilleri[d], V. Cavasinni[a], G. Collazuol[b], G. Conforto[h], C. Conta[c], M. Contalbrigo[b], T. Del Prete[a], A. De Santo[a], R. Ferrari[c], M. Fraternali[c], D. Gibin[b], S.N. Gninenko[f], G. Graziani[e], A. Guglielmi[b], E. Iacopini[e], A.V. Kovzelev[f], L. La Rotonda[g], S. Lacaprara[b], A. Lanza[c], M. Laveder[b], A. Lupi[e], F. Martelli[h], M. Mezzetto[b,*], D. Orestano[c,3], F. Pastore[c,3], E. Pennacchio[c,4], R. Petti[c], G. Polesello[c], A. Rimoldi[c], F. Salvatore[a,2], A. Sconza[b], M. Valdata-Nappi[g,5] M. Veltri[h], V. Vercesi[c], S.A. Volkov[f]

[a] *Dipartimento di Fisica, Università di Pisa and INFN, Sezione di Pisa, Pisa, Italy*
[b] *Dipartimento di Fisica, Università di Padova and INFN, Sezione di Padova, Padova, Italy*
[c] *Dipartimento di Fisica Nucleare e Teorica, Università di Pavia and INFN, Sezione di Pavia, Pavia, Italy*
[d] *CERN, Geneva, Switzerland*
[e] *Dipartimento di Fisica, Università di Firenze and INFN, Sezione di Firenze, Florence, Italy*
[f] *Institute of Nuclear Research, INR, Moscow, Russia*
[g] *Dipartimento di Fisica, Università della Calabria and INFN, Gruppo collegato di Cosenza, Cosenza, Italy*
[h] *Dipartimento di Fisica, Università di Urbino and INFN, Sezione di Firenze, Florence, Italy*

Received 20 July 1996

Abstract

Test beam results of the NOMAD electromagnetic calorimeter are presented showing linearity, signal uniformity, energy and position resolution measured in an electron beam. Tests were also performed placing the calorimeter in a magnetic field of 0.4 T. Results on the π rejection obtained using a combined measurement of preshower/electromagnetic calorimeter are found to be in good agreement with the project expectations. Finally the calorimeter response to the muons is discussed.

PACS: 29.40.Vj; 29.40.Ka; 14.60.Pq

1. Introduction

The main goal of the NOMAD experiment is to search for the appearance of tau neutrinos, ν_τ. The detector is located in the CERN West Area and is exposed to the SPS neutrino wide band beam [1]. The NOMAD detector was designed to measure and identify the electrons, muons, photons and hadrons produced in neutrino interactions. The active target consists of 132 planes of drift chambers located in a magnetic field of 0.4 T which allows the determination of momenta of the charged particles. The target is followed by a transition radiation detector (TRD) to enhance e/π separation and by an electromagnetic calorimeter (ECAL) with an upstream preshower detector (PRS). The trigger is provided by two planes of scintillation counters. A veto in front of the magnet rejects upstream neutrino interactions and muons. A hadronic calorimeter and a muon spectrometer placed outside the magnet provide a rough estimate of the energy of the hadronic component in the event and the muon identification, respectively. The whole detector was efficiently operated and took data since 1995 [2].

The ECAL is crucial to accurately measure electron and gamma energies, both to identify the electronic decay channel of the τ produced by the ν_τ and to determine the size and angle of the transverse momenta of the hadrons and leptons produced in all the neutrino interactions: these kinematical variables are essential to distinguish ν_τ from other neutrino interactions.

The design, construction and electronic performance of the ECAL were presented in Ref. [3]. The ECAL consists

* Corresponding author. Fax: +39 49 8277 145; e-mail: mezzetto@padova.infn.it.

[1] Now at CERN.
[2] Now at Università di Pavia, Italy.
[3] Now at Università "Roma Tre", Italy.
[4] Now at Università di Urbino, Italy.
[5] Now at Università di Perugia, Italy.

PII S0168-9002(96)00944-8

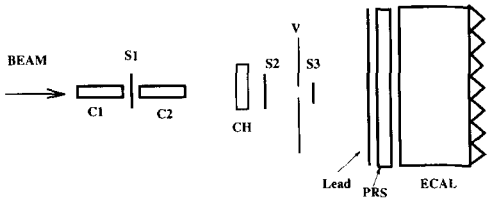

Fig. 1. Test beam setup. C_1, C_2 are Cherenkov counters, S_1, S_2, S_3 are trigger counters, CH is the beam-monitor delay wire chamber, V are the veto counters, PRS is the preshower and ECAL the matrix of lead-glass blocks.

of 875 lead-glass blocks (TF1-000) arranged in a matrix of 35 rows and 25 columns. Each block is $19X_0$ ($\sim$ 500 mm) deep and has a rectangular cross section of 79. $\times$ 112. mm^2. The Cherenkov light produced within the lead-glass is detected by two stage photomultipliers (tetrodes, Hamamatsu R2186) designed to operate in intense magnetic fields and placed at 45° with respect to the axis of the block and to the magnetic field direction to reduce the loss of gain caused by the magnetic field.

Extensive measurements on test beams with different particles have been carried out to fully understand the ECAL response to electrons, charged pions, π^0's and muons. In most cases it was possible to put the detectors inside a magnet providing the same field as in the actual experiment.

A short description of the test beam setups is given in Section 2. In Sections 3 and 4 the energy calibration for electromagnetic (e.m.) showers (electrons and gammas) over an energy range between a few hundreds MeV to 80 GeV are presented, followed by the results on the energy resolution in Section 5. Since the particles generated by neutrino interactions in NOMAD enter the lead-glass blocks uniformly distributed over the front face and with incidence angles up to several tens of degrees, the test beam conditions were steered or the test setups translated or tilted to study the signal dependence on the impact point and on the incidence angle: this is discussed in Sections 6 and 7. PRS and ECAL signals together allow a considerable e/π separation: the π rejection obtained from the test beams analysis is presented in Section 8. Finally, Section 9 describes how to account for some geometrical effects on the signals generated by muons crossing the ECAL. This is necessary in order to use their signal as a monitoring tool, auxiliary to the LED system [4].

2. Test beam setup

Two experimental arrangements are reported. The first measures the performance of the ECAL to electrons in the energy range from 10 to 80 GeV and uses the X5 beam line at the CERN SPS. The second exploits the T9 PS beam line to study the calorimeter response at low energies (1 to 10 GeV). A sketch of the T9 test beam setup is shown in Fig. 1. The beam trigger was defined by the coincidence signal of three scintillation counters, S1, S2, S3. The beam

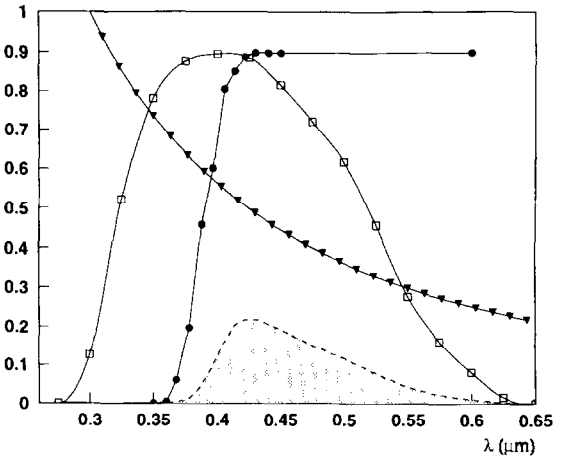

Fig. 2. Cherenkov spectrum of photons emitted by e.m. showers in arbitrary units (triangles); photocathode quantum efficiency (QE) in arbitrary units (squares); glass transmission coefficient for $10X_0$ length (dots). The dashed line represents the spectrum of the photons reaching the photocathode, convoluted with the QE and normalized to the initial Cherenkov spectrum.

halo was vetoed with a scintillation counter (V) in anticoincidence with the trigger counters; the resulting e^- beam spot had 1.5 cm diameter. Since T9 provides an unseparated beam, electrons were identified by two threshold Cherenkov counters, C1, C2. The beam divergence was kept less than 10 mrad. The x and y coordinates of the incoming particles were measured by a delay wire chamber, with 200 μm resolution, placed approximately 1 m upstream the calorimeter. In order to prevent charge pile-up in the amplifier chain, events were rejected if a second particle arrived 20 μs before the trigger.

The X5 test beam setup was essentially the same.

The momentum bite $\Delta p/p$ was about 1% both at X5 and T9 beams.

Several different block matrices were used, sometimes placed inside a magnet that provided the same transverse magnetic field B = 0.4 T as in NOMAD. Both the tetrodes and the electronic chain were the same and operated in the same way as in NOMAD.

The e/π rejection and the π^0 mass measurements were performed with a preshower in front of ECAL as it will be more extensively described afterwards.

During the run periods the stability of the tetrode gain, electronics and pedestals was regularly checked.

3. Energy scale

It is often claimed that the energy response of e.m. calorimeters is linear within a few percent. Deviations from this behaviour occur in calorimeters of finite size, since both the longitudinal and the transverse size of the shower increase with energy and so does the energy leakage. In the case of lead-glass calorimeters linearity is expected because

for an e.m. shower the total track length of charged particles above the Cherenkov emission threshold is proportional to the energy. The details of the propagation, collection and conversion of the Cherenkov photons may spoil the expectation of a perfectly linear response.

The lead-glass is not a perfectly transparent medium: it is opaque in the ultraviolet region (where the Cherenkov emission is more intense) and becomes transparent above $\sim$ 0.42 μm where the photocathode quantum efficiency starts decreasing (see Fig. 2). The longitudinal position of the maximum of an e.m. shower depends on its energy and so does the longitudinal tail: the higher the energy the closer the light to the photocathode. This, taking into account the attenuation of the light, suggests a nonlinear increase with energy in the response of the detector.

3.1. Energy scan

To detect significant deviations from linearity a lead-glass module (10×5 blocks) was exposed first to the T9 electron beam at energies from 1.5 to 10 GeV and later at energies from 6 to 80 GeV to the X5 beam.

Three different sets of runs were performed, centering respectively the electron beam on each of three blocks (called T37, T27, T18) of the module. The three blocks were chosen in such a way that each of them was the center of an array of 3×3 blocks (nonet). In the analysis clusters were built grouping blocks adjacent to the one under study, provided the signal in these blocks was larger than $2\sigma_{\mathrm{ped}}$, σ_{ped} being the pedestals width. The total energy deposited in the nonet (in units of ADC counts) was then plotted as a function of the incident electron beam energy.

The data show that the two scans in the PS and SPS energy regions agree within 1% in the common region ($\sim$ 10 GeV) and each of the two sets is consistent with a linear fit (with deviations $\leqslant$ 1.5%). However, their slightly different slopes prevent the possibility of a good linear fit over the full energy range. This is clearly seen in Fig. 3, which shows the percentage deviations of the points from a linear fit, as a function of the incident energy.

In the hypothesis of a linear response, the single block energy E_i^{bl} would be evaluated from the pedestal subtracted ADC counts ADC_i:

$$E_i^{\mathrm{bl}}(\mathrm{GeV}) = \frac{\mathrm{ADC}_i}{\mathrm{CALIB}_i} E_0^{\mathrm{bl}}(\mathrm{GeV}), \tag{1}$$

where CALIB_i are the ADC counts measured in the calibration procedure, when a 10 GeV electron beam was fired perpendicularly to the center of each block. $E_0^{\mathrm{bl}} = 9.3$ GeV is the energy released, on average, in the single block during this calibration run. In doing so one assumes that the ECAL energies belong to a straight line (the calibration fit) passing through the (E_0, CALIB_i) and the (0,0) points. The cluster energy E_{Cl} is calculated as $E_{\mathrm{Cl}} = \sum_i E_i^{\mathrm{bl}}$, where the calibration energy is now $E_0 = 10$ GeV and the sum is over 9 blocks.

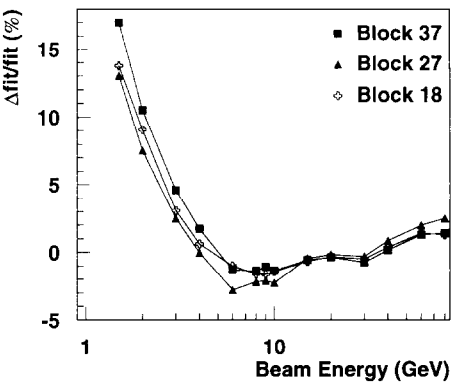

Fig. 3. Deviations from the linear fit as function of the beam energy for the three measured blocks.

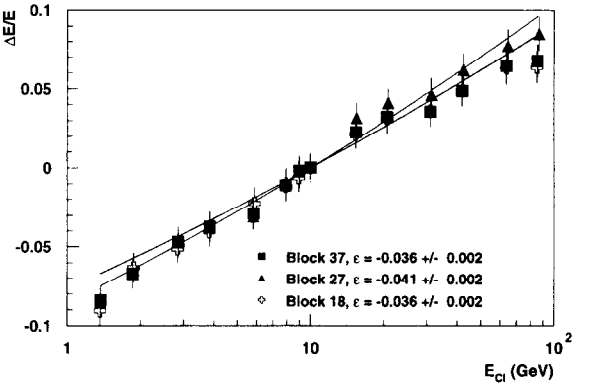

Fig. 4. Deviations from the calibration fit fitted to Eq. (2) for 3 different blocks.

To account for deviations from linearity, the following equation is used:

$$E'_{\mathrm{Cl}} = \frac{E_{\mathrm{Cl}}}{1 + \epsilon \log E_{\mathrm{Cl}}/E_0}, \tag{2}$$

where the only parameter ϵ takes into account all the nonlinear effects over the entire energy range.

The validity of Eq. (2) and the value of ϵ were studied by measuring the energy deviations obtained subtracting the nominal beam energy E_{beam} from the uncorrected cluster energy E_{Cl}:

$$\frac{\Delta E}{E} = \frac{E_{\mathrm{Cl}} - E_{\mathrm{beam}}}{E_{\mathrm{beam}}} \tag{3}$$

In Fig. 4 the plot of $\Delta E/E$ is shown as function of E_{Cl}.

The approach of a single parameter over the full energy range appears to be well supported by the data and provides the average value:

$$\epsilon = 0.038 \tag{4}$$

in good agreement with the Monte Carlo predictions.

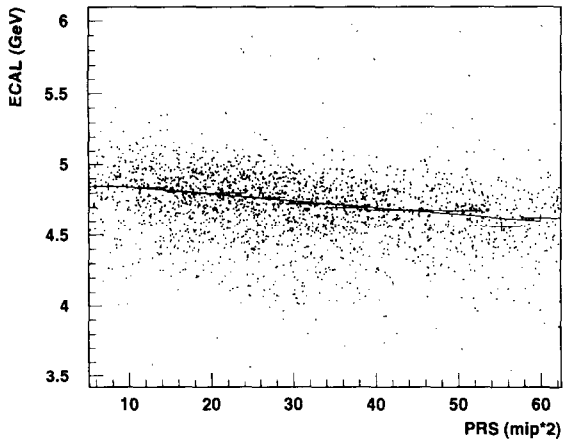

Fig. 5. 5 GeV electron ECAL signals (sum over a nonet) vs. PRS signals (horizontal plane + vertical plane, each plane normalized to one mip). The single events are shown as well as the profile histogram and its linear fit.

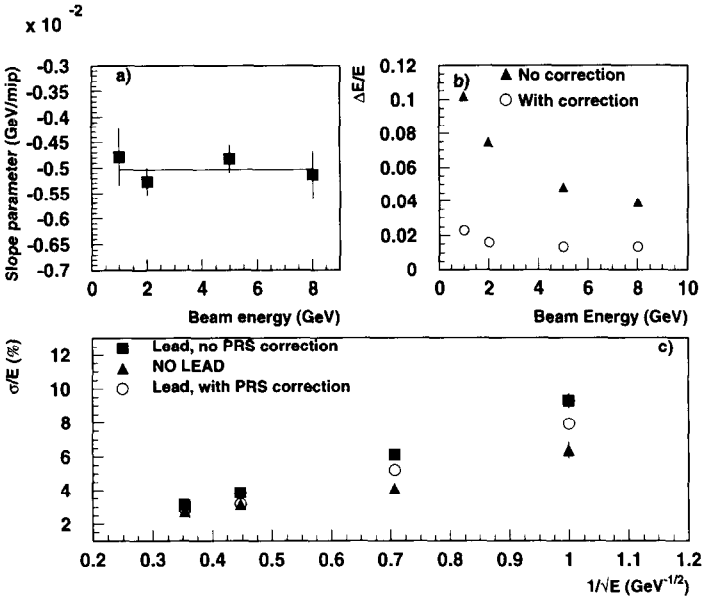

Fig. 6. (a) Values of the slope parameter of the ECAL–PRS linear correlation as a function of the beam energy. (b) Fractional reduction of the ECAL signal, $\Delta E/E$, due to the lead as a function of the beam energy, with and without PRS correction (white circles and black triangles, respectively). (c) Energy resolution as a function of the beam energy without lead (black triangles), with lead and no PRS correction (black squares) and with lead and PRS correction (white circles).

3.2. *PRS–ECAL signal correlation*

In NOMAD a preshower (PRS) made of $1.6X_0$ plane of lead followed by two orthogonal planes of proportional tubes is placed upstream ECAL. This amount of material degrades the ECAL performances, but a compensation can be obtained combining PRS with ECAL signals.

The ECAL–PRS correlation has been measured using electrons of 1, 2, 5, 8 GeV, in a field of $B = 0.4$ T. The PRS used in this test beam was made by a lead layer, $1.6X_0$ deep, followed by two orthogonal planes of proportional tubes $1 \times 1 \times 10$ cm^3, 10 tubes per plane. Each plane signals are normalized to one mip.

Fig. 5 shows the anticorrelation between the PRS and ECAL signals at 5 GeV. When the e.m. shower develops earlier in the lead, the PRS signals are higher and the ECAL signals are slightly lower. The distribution, reduced to a profile histogram, has been fitted with a linear function whose slope parameter b can be used to correct the ECAL signal:

$$E'_{\mathrm{Cl}} = E_{\mathrm{Cl}} - b\mathrm{PRS}. \tag{5}$$

The b values shown in Fig. 6a at different energies are compatible with a constant value:

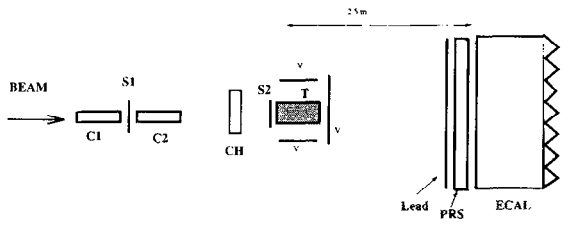

Fig. 7. π^0 test beam setup. C_1, C_2 are Cherenkov counters, S_1, S_2 are trigger counters, CH is the beam-monitor delay wire chamber, T is the polyethylene target, V are the veto counters, PRS is the preshower and ECAL the matrix of 49 lead-glass blocks.

$$b(\mathrm{GeV mip}^{-1}) = -(5.1 \pm 0.2) \times 10^{-3} \quad (\chi^2/\mathrm{n.d.f.} = 0.7). \tag{6}$$

Fig. 6b shows the fractional reduction of the average ECAL signal due to the presence of lead defined as

$$\Delta E/E = (\langle E_{\mathrm{NoLead}}\rangle - \langle E_{\mathrm{Lead}}\rangle)/\langle E_{\mathrm{NoLead}}\rangle, \tag{7}$$

where $\langle E_{\mathrm{Lead}}\rangle$ and $\langle E_{\mathrm{NoLead}}\rangle$ are the average values of the ECAL signals with and without the presence of the PRS.

When the correction function (5) is applied the signal reduction is $\sim 1.6\%$. This effect is well reproduced by Monte Carlo calculations that predict a signal loss of about 1.8%. The reason is due to the light attenuation in the glass related to the early development of the e.m. shower due to the presence of the lead. The final algorithm to combine PRS and ECAL signals is

$$E(\mathrm{GeV}) = (1 - b\mathrm{PRS(mip)})1.016E_{\mathrm{Cl}}(\mathrm{GeV}). \tag{8}$$

The resolution σ/E as function of $1/\sqrt{E}$ is shown in Fig. 6c for three different cases: no lead and $1.5X_0$ of lead with and without the correction function of Eq. (8). It can be noticed that the PRS correction improves the energy resolution approaching the bare ECAL resolution.

4. π^0 mass measurement

The energy scale function of Eq. (2) and the PRS correction function of Eq. (8) were obtained with electrons of energies greater than 1 GeV. To check if these corrections apply also to gammas and to extend their energy range down to 300 MeV, π^0 test beam measurements were performed.

4.1. Experimental setup

Fig. 7 shows a sketch of the experimental setup. π^0 were produced by charge-exchange interactions of a 3 GeV π^- beam in a polyethylene target (5×6 cm^2 cross section, 10 cm long). The probability of this interaction in the target is of the order of 10^{-3}. A preshower made of a lead layer, $1.7X_0$ thick, followed by 2 orthogonal planes of scintillation counters, 24 vertical and 18 horizontal, $3 \times 1 \times 80$ cm^3, was

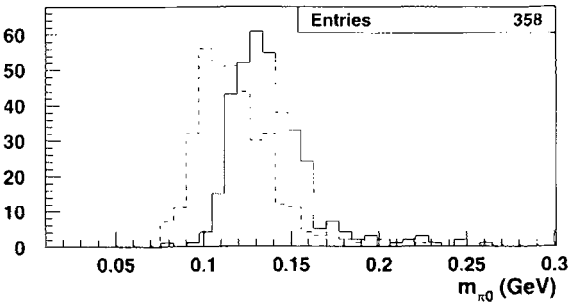

Fig. 8. m_{π^0} distribution without any correction (dashed line) and with the PRS and nonlinearity correction (solid line).

located 2.5 m downstream the target just in front of ECAL. The scintillation counters were instrumented with a $\frac{1}{2}''$ PMT at one end and the signals were fed into charge ADC's.

The central block of the calorimeter module (10×5 blocks), corresponding to the beam impact point, was removed in order to reduce the background due to pion interactions in ECAL.

4.2. Calibration and selection criteria

The PRS signals were calibrated using 3 GeV π^-'s. The mip peak of each scintillator was used as calibration constant.

The ECAL module was calibrated with 6 GeV electrons, without lead in front. The γ directions were determined from the PRS signals; the γ energies were computed by means of Eq. (2) and Eq. (8) combining ECAL and PRS signals.

π^0 events were selected requiring only two energy clusters in the calorimeter. Each cluster was required to have more than 300 MeV and an associated PRS signal larger than 4 mip in each plane. Moreover the sum E of the energies of the 2γ was required to be 2 GeV $\leqslant E \leqslant$ 3 GeV.

4.3. Results

Fig. 8 shows the distribution of the resulting 2γ invariant mass which gives:

$$m_{\pi^0} = (133.7 \pm 1.2)\ \mathrm{MeV} \tag{9}$$

with a $\sigma = 16$ MeV.

5. Energy resolution

Many effects, both of statistical and systematic origin, contribute to the fluctuations of the energy measured in the calorimeter.

The statistical contributions are mainly related to the fluctuations of the energy deposition in the calorimeter and of the number of detected photoelectrons, while the systematic ones are due to the spread and uncertainty in the beam mo-

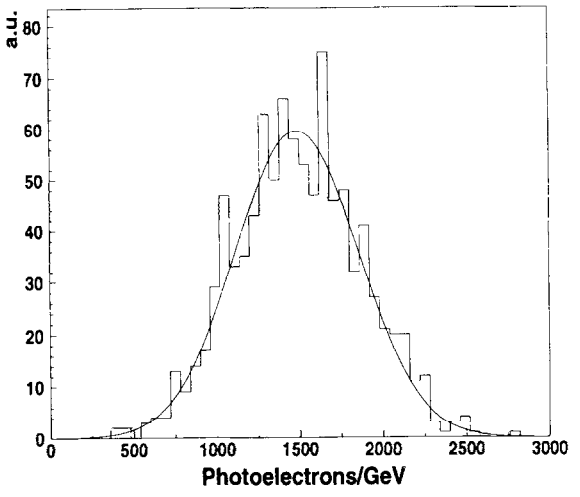

Fig. 9. Photostatistics calculated from LED signals.

mentum and to the incomplete accounting of the lateral and longitudinal energy leakage.

Another contribution arises from the intrinsic noise of the electronic chain. Its value is estimated to be around 12 MeV for each block, as deduced from the widths of the pedestal distributions.

In the following, the contribution to the measured energy width from the momentum bite ($\Delta p/p = 1\%$) is subtracted in quadrature.

5.1. Photostatistics

The number of photoelectrons/GeV is obtained from the signals of the two Light Emitting Diodes (LED1 and LED2), used in the monitoring system and placed at two different positions in the lead-glass back face, under the assumption that their light emission has a poissonian behaviour.

After subtracting the contribution of the electronic noise, the r.m.s. of the signal distribution for each LED is only due to statistical fluctuations of the photocathode emission and of the electron multiplication process in the two tetrode dynodes.

If $T = GN$ is the signal distribution induced by a LED, where G is the tetrode gain (mean value μ_G) and N the total number of photoelectrons (mean value μ_N), then:

$$\left(\frac{\sigma_T}{T}\right)^2 = \left(\frac{\sigma_N}{\mu_N}\right)^2 + \frac{1}{\mu_N}\left(\frac{\sigma_G}{\mu_G}\right)^2. \tag{10}$$

G results from the convolution of the emission in both dynodes. Assuming that they have an ideal poissonian emission ($\mu_1 = \mu_2 \equiv \sqrt{G}$) we get:

$$\left(\frac{\sigma_G}{\mu_G}\right)^2 = \frac{1}{\mu_1} + \frac{1}{\mu_1\mu_2} \equiv \frac{1}{\sqrt{G}} + \frac{1}{G}. \tag{11}$$

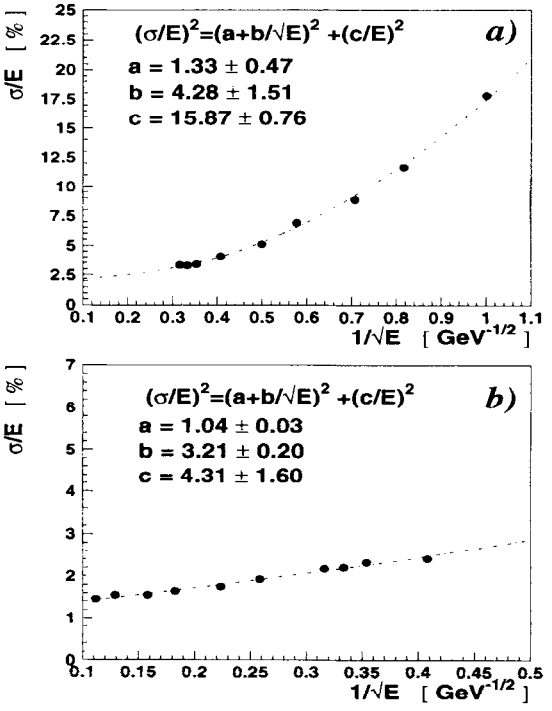

Fig. 10. Energy resolution in a nonet for two different energy ranges: (a) 1–10 GeV at the PS test beam, (b) 6–80 GeV at the SPS test beam.

The photoelectron contribution to the resolution becomes:

$$\left(\frac{\sigma_T}{T}\right)^2 = \frac{1}{N}\left(1 + \frac{1}{\sqrt{G}} + \frac{1}{G}\right). \tag{12}$$

The correction factor for the dynode statistical fluctuations is in the range 0.15–0.27 when we consider the individual gains of all the tetrodes used in the calorimeter (operated at 800 V).

The number of photoelectrons/GeV is obtained from Eq. (12) using the individual gains as given by Hamamatsu after normalizing the LED signals to 1 GeV electrons. The distribution for all blocks, shown in Fig. 9, gives a mean value of $\sim$ 1430 photoelectrons/GeV with an r.m.s. of about 350. The RMS is dominated by the tetrode to tetrode variation of the photocatode quantum efficiency and by the variation of the transparency of the lead-glass blocks.

5.2. Results

Test beam results show that an electromagnetic shower is contained laterally in a matrix of nine blocks with a very small leakage amounting to 0.5% at 80 GeV.

The Monte Carlo simulation was used to estimate the leakage fraction escaping longitudinally from the blocks. This fraction depends logarithmically on the electron energy as expected and its contribution ranges from 0.1% at 1 GeV to 1.9% at 80 GeV.

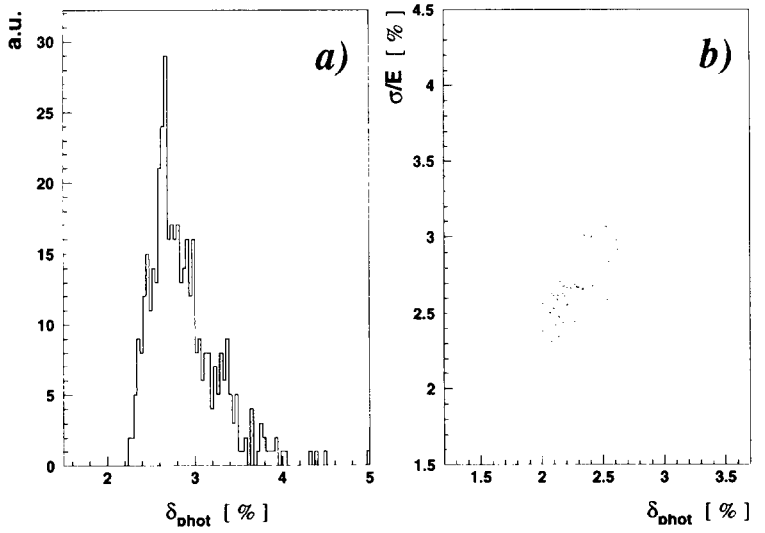

Fig. 11. (a) Statistical contribution to the resolution from photoelectrons (δ_{phot}) and (b) its correlation with the measured resolution.

A three-parameter fit was first used to evaluate the energy resolution:

$$\sigma(E)/E = \sqrt{\left(a + \frac{b}{\sqrt{E}}\right)^2 + \left(\frac{c}{E}\right)^2}, \qquad (13)$$

where the third term is related to the equivalent electronic noise (GeV) and can be factorized as $c = c_0\sqrt{n}$, under the hypothesis of incoherent noise and assuming the same behaviour for all the n blocks used in the analysis.

The energy resolution was studied in the range between 1 and 80 GeV using $n = 9$ (a nonet) and comparing the two independent measurements obtained at the PS and SPS test beam setup. The results, displayed in Fig. 10a and b, show that the constant and the statistical term of the two data sets are compatible within the estimated errors. The electronic noise, on the contrary, is much higher for the PS data as confirmed by the larger pedestal width in the PS measurements.

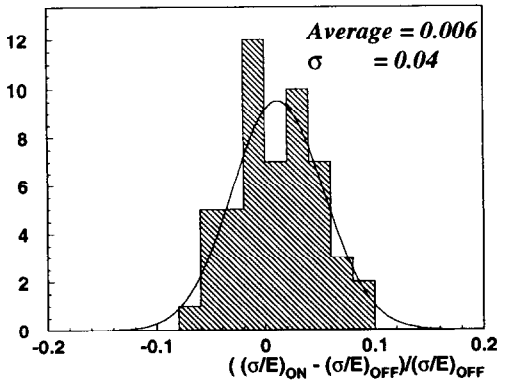

Fig. 12. Effect of the magnetic field on resolution.

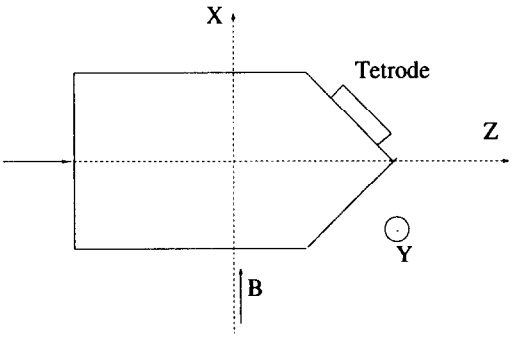

Fig. 13. Schematic structure of a NOMAD lead-glass.

The compatibility of the two data samples allows one to consider in the following only results from the SPS test beam data for which the experimental environment is much cleaner.

The results of the fit are: $a = (1.04 \pm 0.03)\%$, $b = (3.2 \pm 0.2)\%\,\mathrm{GeV}^{1/2}$, $c = (4.3 \pm 1.6)\%\,\mathrm{GeV}$. The third term ($c$) is in reasonable agreement with the electronic noise ($c_0\sqrt{n}$) as evaluated in independent measurements from the r.m.s. of the pedestals (on average $c_0 = 1.4\%\,\mathrm{GeV}$ for the considered blocks).

This consideration leads to a two-parameter fit after the deconvolution of the electronic noise from the data. This fit gives a constant term $a = (1.04 \pm 0.01)\%$ and a statistical term $b = (3.22 \pm 0.07)\%\,\mathrm{GeV}^{1/2}$ when summing over 9 blocks, in good agreement with the three-parameter fit.

The value of b found in the case of $n = 1$ ($b = 3.3\%\,\mathrm{GeV}^{1/2}$ after the deconvolution of the electronic noise) can be used to estimate the value of the statistical term for all the calorimeter blocks. In fact, considering that

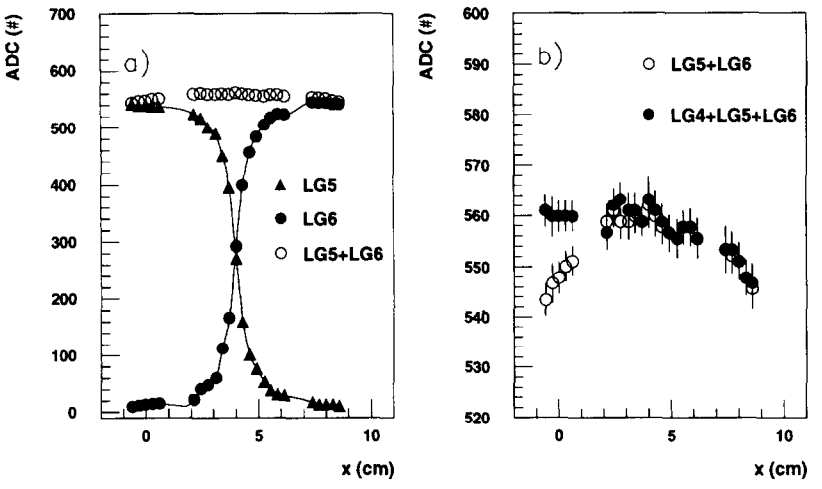

Fig. 14. (a) Results of the horizontal position scan performed with 6 GeV e^-, B off, between the center of LG5 ($x = 0$) and the center of LG6 ($x = 7.9$ cm). The lines are drawn to guide the eyes. (b) The same results with an expanded scale and compared to the 3 blocks sum.

the two main contributions, the photostatistics (δ_{phot} defined in Eq. (12)) and the fluctuations in the energy deposition (δ_{en}) are independent, according to:

$$b = \sqrt{\delta_{\text{phot}}^2 + \delta_{\text{en}}^2} \tag{14}$$

a value for δ_{en} of the order of 1.4% is found, since in the tested block δ_{phot} is equal to 3.0%. The distribution of δ_{phot} for all the calorimeter blocks, presented in Fig. 11a, provides a mean value of 2.9% and a standard deviation of 0.4%: this contribution is expected to be largely dominant for a lead-glass detector as can also be seen from its correlation with σ/E in Fig. 11b. Assuming the same systematic effects for all the blocks (i.e. the same value for the constant term a and the same statistical contribution from the energy fluctuations δ_{en}), the final estimate for the average value of b in single blocks is then $(3.2 \pm 0.3)\%\,\text{GeV}^{1/2}$.

The effect of the magnetic field on the energy resolution was also checked. For a sample of 52 glass blocks the change in resolution at 10 GeV between $B = 0$ and $B = 0.4$ T was measured. The average change, 0.006 ± 0.005, is consistent with zero (Fig. 12).

6. Signal uniformity

Monte Carlo calculations foresee a uniform response of ECAL to electromagnetic particles in spite of the asymmetry of the geometrical layout in the lead-glass/tetrode coupling (Fig. 13). In fact about half of the e.m. shower light comes from electrons below the critical energy, whose directions are not correlated to the initial direction of the particle starting the shower. The case is different for a going-through particle as a muon, as will be discussed in Section 9.

Systematic studies were done at the PS T9 and SPS X5 e^- beams in order to test the response uniformity of the calorimeter as a function of the impact point and the incidence angle of the incoming particles. Measurements were done using e^- beams between 2 and 10 GeV, with and without a $B = 0.4$ T transverse magnetic field.

To simulate the preshower effect on the e.m calorimeter in NOMAD, some of the tests were performed using a preshower made of a lead layer 0.9 cm thick followed by a scintillation counter positioned just in front of the blocks.

6.1. Position dependence

A matrix of 3×3 lead-glass blocks (nonet), was tested at the PS T9 test beam with electrons at an energy of 6 GeV. The electron beam was impinging at normal incidence on the nonet front face.

The results of a horizontal scan between the centers of two adjacent blocks of the nonet, LG5 and LG6 ($x = 8$ cm), are presented in Fig. 14. Fig. 14a shows the signals of the two individual blocks and their sum as a function of the e^- impact point coordinate on the lead-glass. The vertical axis of this plot gives the average ADC counts of each lead-glass at the given position, pedestal subtracted and normalized to the value of the central block. Fig. 14b displays, on an expanded scale, the signal obtained summing two and three blocks, respectively. The total signal of the three blocks LG4, LG5 and LG6 is constant to better than $\pm 0.5\%$ and independent of the e^- impact point also at the boundary between the two blocks (crack). Comparing the signal summed over two and three blocks at the center and at the crack, the lateral leakage for a single block can be derived. The leakage is $\sim 2\%$ as expected from Monte Carlo calculations. The energy resolution is $\sigma_E/E \sim 2.7\%$, independent of the electron impact point coordinate.

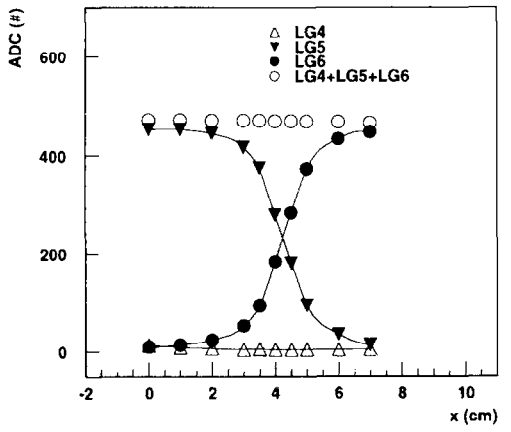

Fig. 15. Horizontal position scan performed with 6 GeV e^- and $B = 0.4$ T.

Selecting electrons hitting very close to the crack (within ± 0.5 mm) a low-energy tail was detected in the output signal distribution summed over two blocks, while the peak value is equal to that measured in the center of the block. This effect is generated by particles entering almost at normal incidence in the crack and propagating a few centimeters in the wrapping material. The crack position and its width are well represented by the distribution of the impact point on the front surface of the block for the events belonging to the low-energy tail. The σ of the distribution is of the order of 600 μm to be compared with the thickness of the wrapping amounting to 250 μm.

Uniformity tests were performed placing the lead-glass nonet in a uniform magnetic field $B = 0.4$ T oriented with respect to the tetrodes as in NOMAD. In this condition, as discussed in Ref. [3] the tetrode response is no longer uniform over the whole photocatode surface; however no degradation in the performance was observed as shown in Fig. 15.

Similar results were also obtained with an e^- beam of lower energy (2 GeV) and the preshower placed in front of the lead-glass blocks.

In conclusion the ECAL is hermetic, except for the very unlike case in which particles are impinging perpendicularly to the front face at ± 0.5 mm around a crack.

6.2. *Angular dependence*

An angular scan of the ECAL response to the SPS X5 e^- beam ($E_e = 10$ GeV) was performed placing three lead-glass blocks (triplet) in a magnetic field oriented with respect to the tetrodes as in NOMAD.

The whole triplet was rotated around the vertical axis in 5° steps pivoting on the center of one of the lateral blocks in order to have better shower containment at large angle. Data were taken with $B = 0$ and $B = 0.4$ T.

Fig. 16a, b show the signals summed over the three blocks: a decrease of 2% when $B = 0.4$ T and of 4% when $B = 0$ T

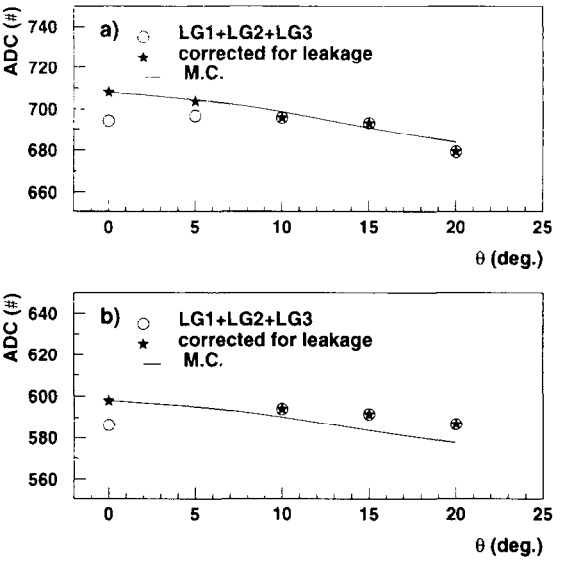

Fig. 16. Signal of 10 GeV electrons as function of the incidence angle θ with $B = 0$ (a) and $B = 0.4$ T (b). Monte Carlo data are normalized to the measured point at 0°.

is observed as the incidence angle θ increases from 0° to 20°. Data at small angles ($\theta \leqslant 5°$) should be corrected for a lateral leakage amounting to $(2 \pm 0.5)\%$. A systematic error due to the uncertainties in the corrections and in the triplet position was estimated to be of the order of (0.7–1.0)%. The Monte Carlo results, also shown in the previous figures, predict a decrease of 3.4% at $\theta = 20°$. This decrease can be explained by the loss in the efficiency of propagation of the light emitted by the core of the shower [6] and by the larger absorption of the light due to the increased distance between the shower and the tetrode.

The dependence of the measured amplitude (energy) from the incidence angle can be empirically described by the relation:

$$E = E(\theta)/\sqrt{\cos(\theta)}. \tag{15}$$

Given the rather good agreement between data and Monte Carlo it is possible to use the Monte Carlo predictions to extrapolate this relation to any incidence angle.

The measured energy resolution, $\sigma_E/E \simeq 2.2\%$, is also independent of the incidence angle.

7. Space resolution

The simplest and most natural method to determine the shower position in hodoscopic calorimeters is the center of gravity method:

[6] The Cherenkov cone produced by tracks parallel to the axis is propagated by total internal reflection while for tracks at an angle with the axis a fraction of the Cherenkov cone touches the side walls at an angle greater than the critical angle and is less efficiently propagated.

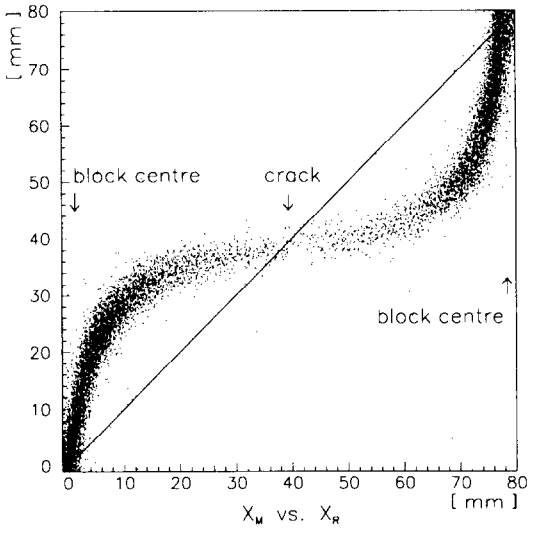

Fig. 17. Correlation between measured and reconstructed position in the x direction.

$$X_R = \frac{\sum_i E_i X_i}{\sum_i E_i} \tag{16}$$

where E_i and X_i are the deposited energy and the coordinate of the center of the ith block, respectively; the sum expands over all the blocks included in the cluster.

A lead-glass matrix (16×4) was irradiated uniformly with 10 GeV electrons over a region of approximately 160×220 mm to measure the space resolution of the calorimeter. The position of incoming particles was measured using a delay wire chamber with 200 μm resolution (see Section 2).

Since the Molière radius for the NOMAD calorimeter compares well with the block dimensions, the largest part of the shower energy is deposited in one block. As a consequence, a nonlinear relationship between the measured and reconstructed positions is observed both in x and y directions as shown in Fig. 17, giving a large bias in the position estimate.

In order to remove such systematic effects a fit to these data can be performed using the function:

$$X_M = a_1 + a_2 \tan(a_3 X_R + a_4), \tag{17}$$

where X_M and X_R are the measured and the reconstructed position, respectively. The residual distributions (Fig. 18a, b) are symmetric and no systematic shifts remain after corrections. Since the fluctuations in the original reconstructed position X_R are small, this algorithm provides a good overall resolution of the order of 4 mm in both x and y directions.

The space resolution is also expected to be a function of the position with respect to the center of the block, the shower containment being a factor that can increase the measured fluctuations in energy deposition. This behaviour is shown in Fig. 19 for the y direction, where a factor of 3 variation is found between the center and the edge of the block.

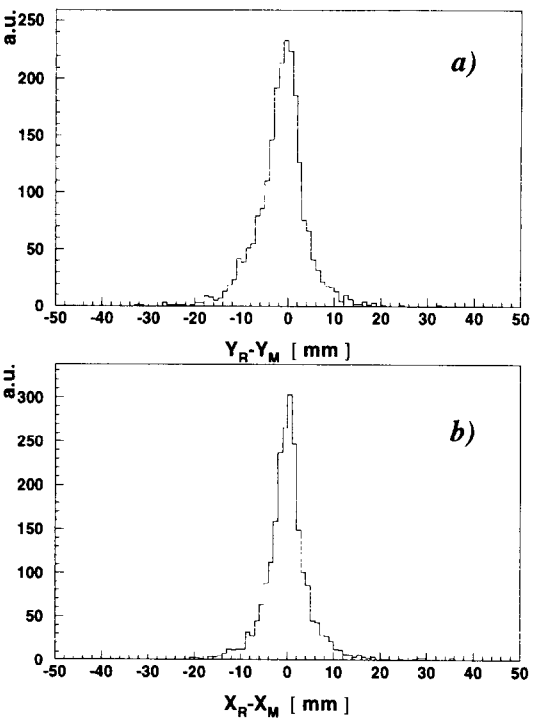

Fig. 18. Difference between measured and reconstructed position after the corrections of Eq. (17) (see text).

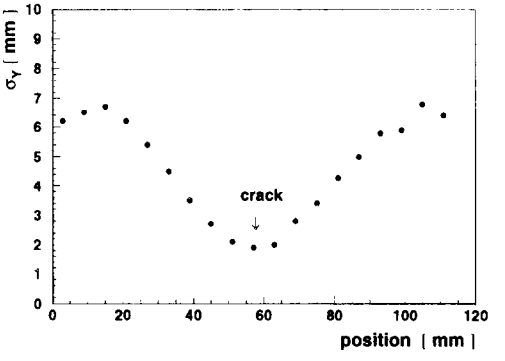

Fig. 19. Space resolution as a function of the position inside the block.

The position resolution is observed to slightly worsen with the incidence angle of the particle, due to the additional fluctuations coming from the longitudinal shower profile for $\theta \neq 0°$.

8. π rejection

The PRS and the ECAL signals can be used to separate electrons from pions. The test beam setup for these measurements is the same of the setup discussed in Section 3.2.

The PRS signals, expressed as sum of horizontal and vertical planes, both normalized to one mip, for 5 GeV pions and

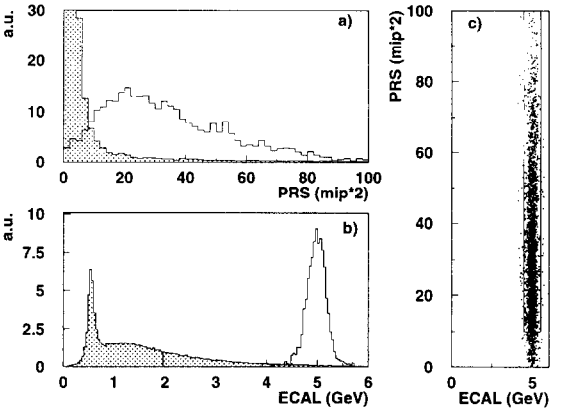

Fig. 20. 5 GeV π (shaded) and electron signals on the PRS (a) and on ECAL (b). PRS vs. ECAL signals for 5 GeV electrons (c), the limits shown in this figure define the 90% efficiency region for electrons detection.

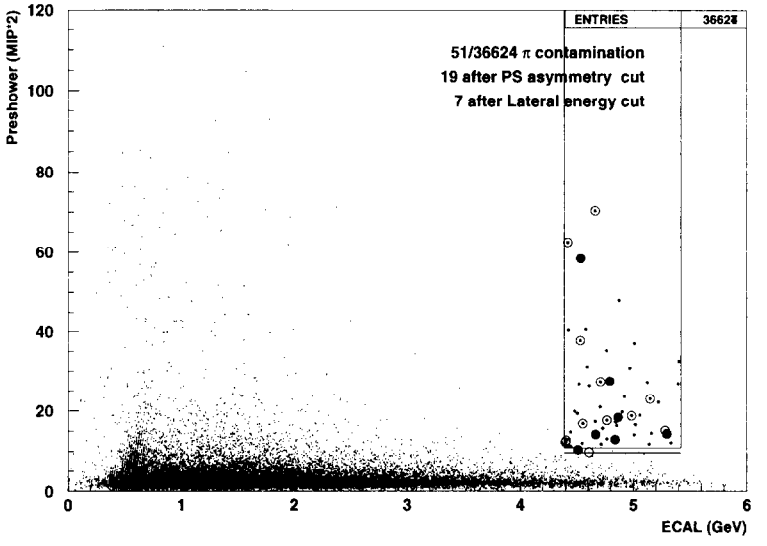

Fig. 21. PRS vs. ECAL signals for 5 GeV π's (small dots). The events falling in the 90% efficiency region for electrons (solid lines) are marked with big dots, while the events surviving the PRS plane asymmetry cut and the cluster shape cut are marked by circles and black circles, respectively. The lower horizontal line represents the recalculated 90% efficiency limit on PRS to take into account the effect of the PRS plane asymmetry cut on electrons.

electrons are shown in Fig. 20a; the energies deposited in a ECAL nonet, corrected with PRS signals following Eq. (8), are shown in Fig. 20b; PRS vs. ECAL signals for electrons are shown in Fig. 20c. The 90% electron detection efficiency is obtained when the ECAL signal is within $\pm 3\sigma$ from its mean value and when a proper threshold, $\mathrm{PRS_{THR}}$, is fixed on the same plot for the PRS signal, see Fig. 20c.

Fig. 21 shows the same distribution for π where 51 events out of a sample of 36624 fall in the 90% efficiency region for electrons.

The π contamination can be reduced with a cut on the ratio of the PRS planes signals: a particle is considered to be a π only when the signal in one plane does not exceed the signal of the other by more than a factor of 5. Moreover, by taking into account the cluster shape, a cut was applied requiring that the energy outside the central ECAL block is lower than 0.2 the signal in the central block. Under these conditions the π/e contamination is reduced to $\sim 2 \times 10^{-4}$ without affecting the e^- detection efficiency.

The final π/e rejection, for normal and central incidence, is shown in Fig. 22 as a function of energy.

From the experimental data a parametrization of the $\mathrm{PRS_{THR}}$ energy dependence is obtained ($\mathrm{PRS_{THR}}$ is given in units of mip).

It turns out that

$$\mathrm{PRS_{THR}}(E) = 3.2 + 1.35E(\mathrm{GeV})\ (\mathrm{mip}), \qquad (18)$$

when the cut on the ratio of the two planes is not used and

$$PRS_{THR}(E) = 2.3 + 1.3E(\text{GeV}) \text{ (mip)}, \quad (19)$$

when the cut on the ratio of the two planes is used.

9. Muon signal

The NOMAD experiment collects about 20 muon triggers between the two neutrino spills in each SPS cycle for alignment and calibration purposes. These muons can be used to monitor the calorimeter response in parallel with the LED system [4] since the value of their signal peak is approximately energy independent in their energy range (from 5 to 50 GeV).

The muon signal in the lead-glass is mainly due to the Cherenkov light emitted by the muon itself, giving a number of photoelectrons corresponding to an energy of about 0.55 GeV (see Fig. 23).

However, the particular block geometry together with the asymmetry in the light detection caused by the phototetrode position (Fig. 13) introduces a dependence of the signal

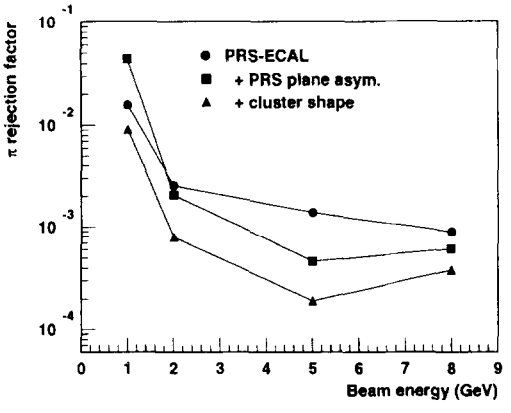

Fig. 22. π/e rejection factor, for 90% electron detection efficiency, as function of the beam energy.

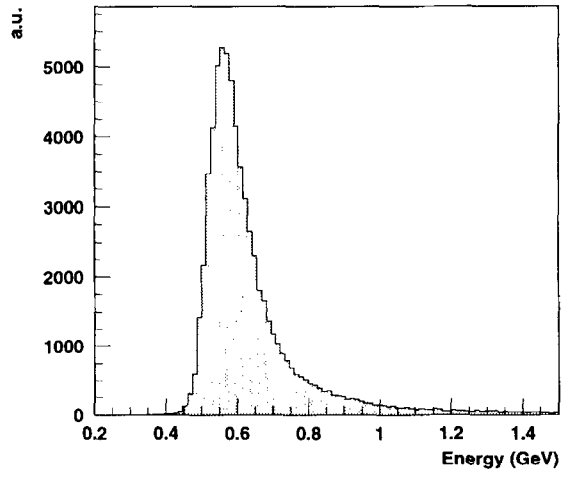

Fig. 23. Muon signal in the calorimeter.

Table 1
Muon peak values (MeV) with and without correction at different impinging angles

	$\theta_x = 0$ mrad	$\theta_x = 30$ mrad	$\theta_x = 60$ mrad
Raw	536.2 ± 4	521.8 ± 4	508.8 ± 5
Corrected	560.0 ± 5	566.0 ± 4	563.0 ± 4

S from the position and the angle of incidence of a muon hitting the calorimeter:

$$S = S(\theta_x, x, \theta_y, y). \quad (20)$$

Therefore, in order to exploit the muon Cherenkov signal to monitor the calorimeter response, it is necessary to correct for this effect. Function S has been parametrized using both Monte Carlo and test beam data.

From Monte Carlo it was observed that S factorizes as follows:

$$S(\theta_x, x, \theta_y, y) = E_0 H(\theta_x, x) K(\theta_y, y), \quad (21)$$

where $H(0,0) = K(0,0) = 1$ and E_0 is the calorimeter signal associated to a muon impinging in the center of the block perpendicularly to the entrance face.

The function K is symmetric under the two transformations $\theta_y \to -\theta_y$ and $y \to -y$ and it was found to be the product of a function $G(|\theta_y|)$ times a quadratic function $g(Y)$ of the linear combination $Y = y + L_y\theta_y$ where $L_y = 70.0$ cm:

$$K(\theta_y, y) = G(|\theta_y|) g(Y). \quad (22)$$

The function H, which is not symmetric, can still be written as the product of a function $F(\theta_x)$ times a function $f(X)$ of the linear combination $X = x + L_x\theta_x$ where $L_x = 53.3$ cm:

$$H(\theta_x, x) = F(\theta_x) f(X). \quad (23)$$

All these functions were parametrized with polynomials and a check of the parametrizations was done using test beam data.

Test beam measurements were performed in the X5 beam using 60 GeV muons impinging on a 16×4 blocks matrix. The position of the incident particle was measured by a delay wire chamber and a complete horizontal and vertical scan for three different incidence angles $\theta_x = 0$, 30 and 60 mrad was performed.

Test beam data were then corrected dividing the measured value by the global correction function

$$G(|\theta_y|) g(Y) F(\theta_x) f(X). \quad (24)$$

Figs. 24 and 25 show the effect of the correction on the signal profiles plotted versus x and y, respectively. Table 1 gives the muon signal peak value (integrated over the block front face) before and after correction, for various θ_x angles. The results are compatible with an E_0 value of 564 ± 4 MeV.

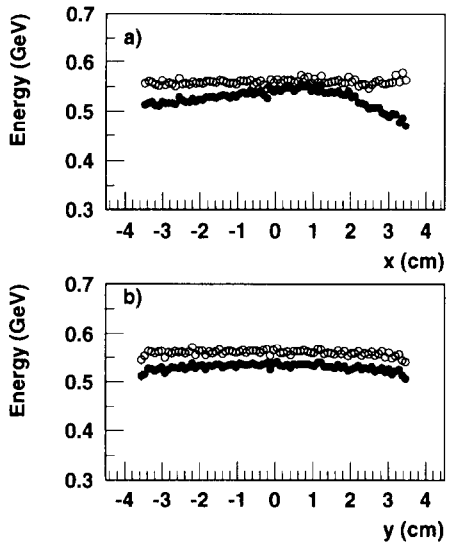

Fig. 24. Horizontal (a) and vertical (b) position scan with 60 GeV muons impinging on the calorimeter front face at 0° degree. Black and open circles represent raw values and values corrected using Eq. (23), respectively.

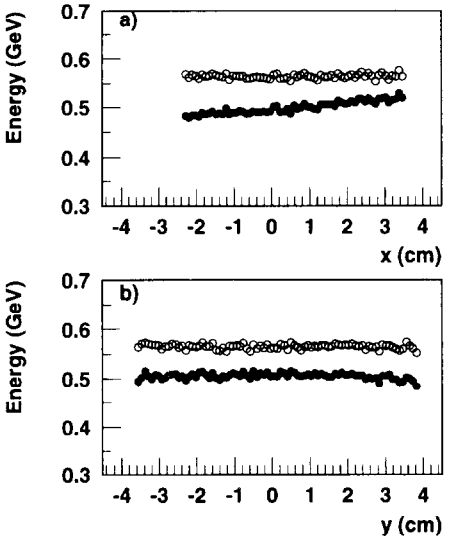

Fig. 25. Horizontal (a) and vertical (b) position scan with 60 GeV muons impinging on the calorimeter front face with an incidence angle θ_x = 60 mrad. Black and open circles represent raw values and values corrected with Eq. (23), respectively.

10. Conclusions

In this paper results on the performance of the NOMAD electromagnetic calorimeter (ECAL) when exposed to electrons, muons and pions test beams were presented. Deviations from linearity in the response of the lead-glass modules were measured in the energy range 1.5–80 GeV; a simple logarithmic term can account for these deviations giving a good energy calibration. The energy calibration was checked by means of the π^0 mass measurement in a special beam setup. The energy resolution σ_E/E was found to have a statistical contribution of $3.2 \pm 0.3\%$ and a constant term of 1%. It was also found that the magnetic field did not affect the energy resolution. Beam scans performed between the centers of two adjacent blocks show that the ECAL is practically hermetic and its response is uniform on the whole block surface. The ECAL response as a function of the impact angle was also measured. Combined measurements of the ECAL with a preshower detector similar to that used in NOMAD, provided an e/π rejection of about 10^{-3} which is perfectly adequate for the requirements of the experiment. Finally, the muon signal in the ECAL was studied: after a correction needed to take into account the block geometry and the asymmetry in the light detection introduced by the phototetrode position, the muon signal was found to be sensitive enough to be used as a monitoring tool, complementary to the LED system.

Acknowledgements

We thank the University of Lausanne for lending us the NOMAD preshower prototype used in the measurements described in the text. The authors wish to thank the technical staff of the Cosenza, Firenze, Moscow, Padova, Pavia and Pisa groups for their invaluable contributions. Special thanks are due to P. Gesuato and A. Vicini for their continuous contributions to the mechanics and to G. Barichello, F. Pellegrino and D. Rizzi for their significant contribution in setting up part of the electronics.

Thanks are due to the CERN staff for their important contributions. We wish in particular to thank W. Huta for his constant help on the electronics.

We are very grateful to L. Di Lella for his collaboration during test beam measurements.

The financial support of INFN and INR is gratefully acknowledged.

References

[1] NOMAD proposal and addenda:
CERN-SPSLC/91-21, CERN-SPSLC/91-48, CERN-SPSLC/91-53, CERN-SPSLC/93-19, CERN-SPSLC/94-21, CERN-SPSLC/94-28.
[2] NOMAD Collaboration, J. Altegoer et al., Contribution to the EPS HEP '95 Int. Conf. on High Energy Physics, August 1995, Brussels, Belgium.
[3] D. Autiero et al., Nucl. Instr. and Meth. A 373 (1996) 358.
[4] D. Autiero et al., Nucl. Instr. and Meth. A 372 (1996) 556.